UNIVERSITY OF CALIFORNIA,
IRVINE

Reactive transport and mineral precipitation in variable-aperture fractures: Comparison of a full three-dimensional model to a depth-averaged two-dimensional model

DISSERTATION

submitted in partial satisfaction of the requirements
for the degree of

MASTER OF SCIENCE

in Civil Engineering

by

Sixue Wang

Dissertation Committee:
Associate Professor Russell Detwiler, Chair
Associate Professor Amir AghaKouchak
Associate Professor Jasper A. Vrugt

2017

DEDICATION

This dissertation is dedicated to my friends and family. Thank you for supporting me in every decision I made, and making my life better.

TABLE OF CONTENTS

LIST OF FIGURES

ACKNOWLEDGMENTS

I would like to thank Professor Russell Detwiler for the professional guidance and extraordinary patience to this research project.

I also want to give special thanks to my thesis committee members, Professor Amir Aghakouchak and Professor Jasper A. Vrugt.

ABSTRACT OF THE DISSERTATION

Reactive transport and mineral precipitation in variable-aperture fractures: Comparison of a full three-dimensional model to a depth-averaged two-dimensional model

By

Sixue Wang

MASTER OF SCIENCE in Civil Engineering

University of California, Irvine, 2017

Associate Professor Russell Detwiler, Chair

Calcium carbonate, which is an important mineral in both anthropogenic and biological systems, is a very critical component in nature. Numerous studies have shown that precipitation of calcium carbonate in fractured and porous media influences solute transport. Previous studies have used two-dimensional computational models to mimic the three-dimensional fluid flow and reactive transport of dissolved mineral. With the goal of improving understanding of mineral precipitation and transport process and to test the accuracy of results from the two-dimensional models, a three-dimensional, two-step reactive transport computational model is developed with OpenFOAM, an open source, C++ based CFD toolbox. This thesis presents the processes of customizing OpenFOAM to solve reactive flow and transport in a three-dimensional variable aperture fracture. Several parameters, including resolution in aperture height direction, aperture fields, and relative roughness of fracture surfaces, are modified to assess sources of errors and to test the soundness of the model. Results are then directly compared with those from the two-dimensional model. Also, a comparison view of different discretization schemes for representing advection in the transport model is presented. All together, our research results suggest that even though false diffusion is observed, the upwind scheme is chosen because of its boundedness and stability.

Chapter 1

Introduction

1.1 Motivation

1.1.1 Mineral precipitations role in nature

Calcium carbonate is an important component in natural systems. Geological carbon dioxide storage, bacteria-induced calcite precipitation in surface and near-surface hydrothermal systems [19], and biochemical products of marine organisms [41]are some applications of calcium carbonate in natural and anthropic systems. Calcium carbonate is also applied to purification of water, and found to be extreme efficient in removing heavy metals with the calcium carbonate extracted from starfish, better than sawdust and active-carbon [28]. Pharmaceutical usage of making calcium alginate hydrogel with the addition of calcium carbonate has been proved to be destroyed easily with ultrasound while keeping an integrated structure under agitation [37]. Studying the formation of calcium carbonate in fractured and porous media can help us better understand not only properties of the subsruface, like transmissivity and heterogeneity, but also the influence on solute transport. Results of

numerous experimental studies have shown the significant role of mineral precipitation in fractured and porous media [40],[26],[61], while only a few three-dimensional computational models have been developed to get insight into this problem [20],[7]. In this thesis, a three-dimensional computational model was developed with OpenFOAM to numerically simulate flow and mineral precipitation in fractured media at the scale of a single fracture.

1.1.2 CO_2 fate, transport and sequestration

The increasing CO_2 concentration in the atmosphere has raised public awareness during recent decades and the stabilization of atmospheric CO_2 has become a pressing issue. Anthropogenic carbon dioxide storage in geological formations has been suggested as a way of sequestration [24],[2]. Geological sequestration of CO_2 entails capturing carbon dioxide from human sources before it is emitted to the atmosphere and then compressing and injecting the CO_2 into underground geological formations [27]. Different mechanisms then act to limit upward migration. These include but are not limited to: structural seals below impermeable caprock, which acts as a barrier that stops carbon dioxide moving into shallower aquifers and acidifying water system [65]; capillary trapping, in other words residual trapping, traps carbon dioxide by capillary forces in the intergranular pore space within rocks [36]; and mineral trapping is where CO_2 is precipitated as solid carbonates[30].

Carbon dioxide, along with methane, are the two main forms of carbon in the Earths atmosphere and important component of the carbon cycle. The geologic carbon cycle is one of the most crucial factors that determines the amount of carbon in the atmosphere [46]. CO_2 in the Earth′s lithosphere is mostly released from the metamorphism process of carbonate rocks in the ocean crust [59]. The model developed in this thesis is directly relevant to the transport of CO_2 in subsurface fractured and porous media. It is suggested that concentration of CO_2 is higher in ground air (air in vadose zone) than soil air for most of the year,

and is definitely a noticeable source of CO_2 [1]. The soil air mentioned above refers to air in phreatic zone. Both soil air and ground air have same composition as air in the atmosphere, and they only different in proportions. With the estimation from Kessler, the annual global flux of inorganic carbon into groundwater is around 0.2 GtC (Gigatonnes of carbon) [35]. Due to this significant amount of CO_2 input into groundwater, it is imperative to study the fate and transport of CO_2 underground. Precipitation of calcite is a common fate of dissolved carbonate [53].

1.1.3 Calcium source and transport

Calcium is among one of the most abundant cations in groundwater [52], and is mainly dissolved from rocks. Other common dissolved mineral substances include magnesium, sodium, bicarbonate, sulfate, and chloride. Another possible source of calcium in groundwater is the recharge from calcareous conditioned wetlands [23]. Along with magnesium, calcium is the most dominant contributor to the hardness of water, and can affect the worth of water for either civil or industrial uses [55]. Excessive intake of calcium can impair human health [52]. These minerals are present in groundwater as a result of bedrock erosion interactions with the atmosphere, and biological metabolism [15]. Since the diffusion coefficients are normally small, advection is the dominant mechanism for the transport of dissolved minerals as well as manmade environmental contaminants [43]. It is also possible that these solutes may travel significant distance underground due to the heterogeneity of subsurface properties. Thus accurately modeling advection is critical to understanding transport and reactions involving calcium and carbonate ions.

1.2 $CaCO_3$ reaction processes

1.2.1 Introduction of calcite, vaterite, and aragonite

Calcite, vaterite, and aragonite are three polymorphs of calcium carbonate. They belong to different crystal systems, and can be converted to each other under certain conditions [6]. The difference between the three polymorphs are the relative position between the carbonate ions and the central calcium ion [6]. Calcite is trigonal, vaterite is hexagonal, while aragonite belongs to the orthorhombic group. Since the properties of each polymorph are different, the control of crystal formation can be very important for industry. As a result, copious research has been conducted to study the conditions and mechanisms of the precipitation of calcium carbonate polymorphs [54]. Many parameters and variable have been determined to qualify the formation of different polymorphs. Cu (II) has been proved to have inhibitive effect on calcite [50]; when controlling $CaCO_3$ morphology, simple ammonium ions play the part as effective additives [21]; SO_4^{2+} and Mg^{2+} impurities in flow can disturb the initial precipitate formation of calcite spheres and make the crystallization process slower than the control test [63]. Among the three polymorphs, calcite is the most common and thermodynamically stable form of calcium carbonate [66]. The molecular structure of calcite can be described with a face-centered rhombohedral model with a calcium atom occupying the center cell, and all six CO_3^{2+} groups lie parallel in abutting layers with opposite directions [5]. As it is the least stable form of calcium carbonate, vaterite has a higher solubility than either calcite or aragonite [51]. This thesis focuses on the fracture surfaces formation of calcite on mineralogically heterogeneous.

1.2.2 Calcium carbonates crystallization mechanism

Different crystals have different growth pathways and the same crystal may have growth different pathways due to variations in nucleation under different saturation conditions [39]. As a result, the final geometry of a crystal depends on the process of crystallization. Crystals can only grow or precipitate from a seed or in other words, a crystal nucleus. Crystal seeds can be treated as a surface, and consist of terraces, which are flat areas, and steps, which are raised layers as shown in Figure 1.1 [8], [9]. Kink sites are the defects on crystal surface to which molecules can be attached more tightly because more bonds can be formed at kink sites [10]. Therefore, the rate of molecules attaching to a crystal surface, i.e. the growth rate of crystal, is proportional to kink density. At larger scales, there are mainly four variables that can control the rate of calcite precipitation; the concentration of calcite, dissolved inorganic carbon concentration, the pH value of the solution, and the availability of nucleation sites [25]. When the ion activity product (IAP) for calcium and carbonate ions is higher than the solubility product, which means the saturation index (Ω) is greater than 1, the solution is supersaturated with calcium carbonate, and calcite will precipitate. In this thesis, a flow with $\Omega = 16$ with respect to calcium carbonate is used as the inflow for the model.

1.2.3 Calcite precipitation kinetics

Knowing the precipitation kinetics and mechanisms of calcium carbonate helps understand and predict mineralization and reactive transport in fractured and porous media. Both transport conditions and surface reactions have impact on calcite growth from a supersaturated solution [67]. For addition, precipitation rate of calcite can be different in different geological systems and geometric conditions [13].

The precipitation process of calcite is accelerated at first with a rapid initial growth rate, and then slows down to a rate that can be described with kinetic rate equations [45]. Due

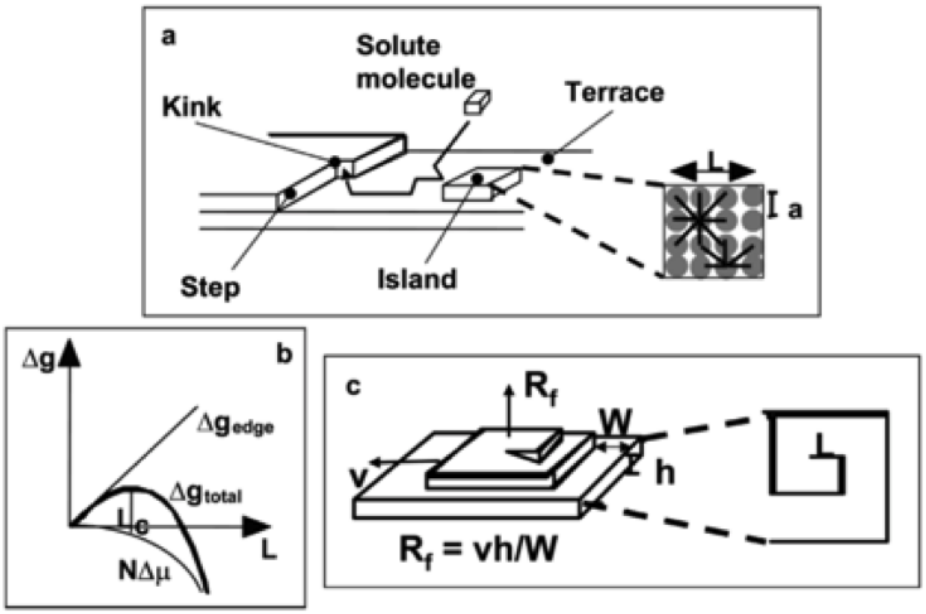

Figure 1.1: Crystal growth illustration. Adapted from "Principles of crystal nucleation and growth", by De Yoreo, J. J., Vekilov, P. G., 2003, Reviews in mineralogy and geochemistry, 54(1), 57-93. Copyright 2017 by the Mineralogical Society of America

to the abundant amount of carbon dioxide in subsurface system, concentration of calcium ions will become the limiting reagent. Numerous studies have shown the importance of the selection of calcium carbonate precipitation rate laws [58]; [32]; [22].

One prevalent equation describing the rate of calcite precipitation under constant temperature is [38]

$$R_{\text{ppt}} = k\left[\left(\frac{IAP}{K_{\text{sp}}}\right)^m - 1\right]^n = k(\Omega^m - 1)^n \tag{1.1}$$

k (mm/s) is the rate constant, Ω is the saturation index ($\Omega = \frac{IAP}{K_{\text{sp}}}$), K_{sp} is the solubility of calcite, and IAP is the ion activity product ($IAP = a_{\text{Ca}^{2+}} a_{\text{CO}_3^{2+}}$, where $a_{\text{Ca}^{2+}}$ and $a_{\text{CO}_3^{2+}}$ are the activities for calcium ion and carbonate ion). Different n and m values can be used to represent different kinetic behaviors of the reaction. When $n = 1$, which is a linear rate law for the precipitation process of calcium carbonate, the equation was used by Nielsen [47] to describe the adsorption of lattice ion; when $n = 2$, growth with spiral mechanism

can be predicted; when $n > 2$, two-dimensional surface nucleation is best represented by the equation [58].

In this thesis, we assume that the calcite precipitation reaction involved in continuum scaled reactive transport modeling is a first-order reaction with a certain precipitation rate to simplify the reaction calculations. However, this model is flexible, and future studies can modify the kinetics into higher-order reaction rate laws to simulate the precipitation of mineral with different growth pathways.

1.2.4 Research objectives

Efficient computational models provide a potentially useful alternative for understanding mineral precipitation and transport processes in the subsurface. Computational models are faster and more economical than lab-scale experiments [42]; [3], and allow efficient exploration of the importance of relevant parameters. In this thesis, a three-dimensional reactive transport model has been developed to study reactive transport during mineral precipitation. Further description of this model will be discussed in the next chapter.

Previously, a two-dimensional computational reactive fluid flow model was developed to represent the three-dimensional fluid flow and reactive transport [11]. The two-dimensional model represents aperture heterogeneity by depth-averaging the flow and reactive treansport equations across the fracture. The objective of this study is to improving understanding of mineral precipitation and reactive transport processes in subsurface flow, and test the accuracy of results from two-dimensional models with a newly developed three-dimensional model from this thesis.

Chapter 2

Methods

2.1 Solvers background

The work presented in this thesis is simulated by a customized model using OpenFOAM® Finite Volume Method (FVM) Computational Fluid Dynamics (CFD) package. FOAM stands for Field Operation And Manipulation. OpenFOAM is an open source multi-physics modeling platform written in C++. It has a flexible modeling environment and extensive range of features that allow solution of a wide range of partial differential equations, involving heat transfer, chemical reactions, combustion, to solid mechanics, and electromagnetics [48]. There are a number of example models developed for commonly solved problems, two of which will be used in this study. The Navier-Stokes equations and continuity equations used in this model are discretized with finite volume method by OpenFOAM [16].

The finite volume method was first used by Evans and Harlow to solve hydrodynamic problems [17]. Finite volume method firstly divides the domain into control volumes, then integrates the differential equation over the control volume and apply divergence theorem. The finite volume method inherently conserves mass, momentum and energy, does not limit the

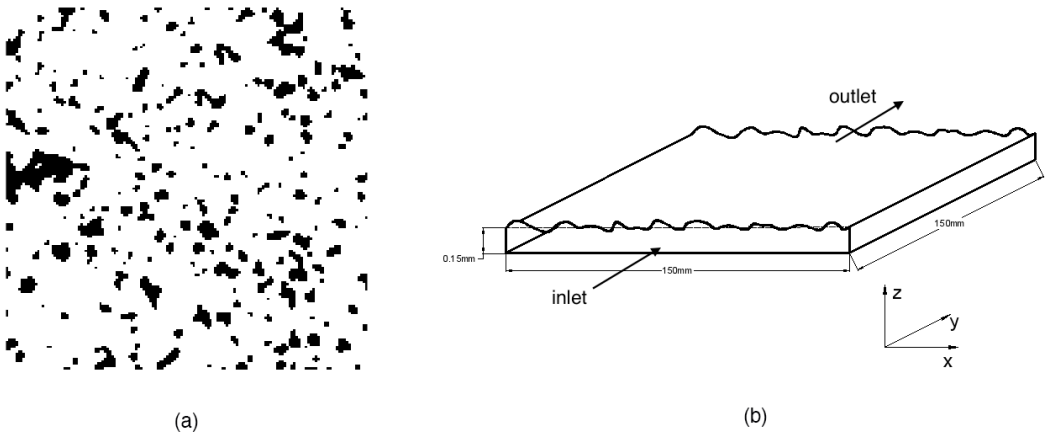

Figure 2.1: (a) Reactive sites location map. Black spots represents reactive regions where calcite seeds are located. (b) Illustration of the model′s geometry.

shape of grid cells, and uses less memory while runs faster than most of the other methods available, like finite element method. Fallah et al. compared the finite volume (FV) method and the finite element (FE) method using a geometrically nonlinear stress analysis, and found that the convergence rate was faster for the FV scheme, while the accuracy remains comparable to the FE scheme [18]. However, one disadvantage is that it might introduce false diffusion when using simple numerical methods; this will be discussed in more detail in section 2 of this chapter.

The model used in this thesis is a two-step model which solves the three-dimensional velocity field first and then uses the results as input to compute the concentration field as the second step. A steady-state solver for incompressible flow called simpleFoam is used to calculate the flow field, and a transient passive scalar transport equation solver called scalarTransportFoam is used to solve the concentration field. Time steps are adjusted to ensure the value of Courant number is below 1 in order to ensure the numerical stability of the reactive transport algorithm.

2.2 Three-dimensional flow and reactive transport model

2.2.1 Velocity field

As the first step of this model, the three-dimensional Navier-Stokes equations are solved. The Navier-Stokes equations consist of a continuity equation, which for incompressible flow is:

$$\nabla \cdot (\rho \vec{U}) = 0 \tag{2.1}$$

and a momentum equation:

$$\nabla \cdot (\vec{U}\vec{U}) = -\frac{1}{\rho}\nabla p + \nabla \cdot (\mu \nabla \vec{U}) \tag{2.2}$$

where μ is the dynamic viscosity of the fluid. Laminar flow model was considered as the flow in subsurface generally occurs at low Reynolds numbers. *Gauss linear* is the gradient scheme picked for the velocity solver. *Gauss* indicates a standard finite volume discretization of Gaussian integration, and it needs the interpolation of variables from cell centers to face centers. *Linear* therefore refers to the interpolation scheme, meaning linear interpolation [60].

Divergence scheme for simpleFoam is *bounded Gauss upwind*. This is the simplest numerical scheme, and easy to apply. The results are very stable, however diffusive where the gradient of targeted variable is high, to put it another way, the scheme tends to smear the sharp gradient as we will show in transport section. It is a first order scheme that includes a ∇U term to help keeping boundedness of target variables and can also improve convergence rate because although ∇U is zero for incompressible flow, $\nabla U \neq 0$ before convergence [60].

Fixed pressure boundary conditions are imposed at the inlet (x=0) and outlet (x=150mm) with a difference of pressure set to be 30 (Pa), which would give a maximum steady velocity around 5.5×10^5 (m/s) that scaled to the velocity used in Jones′ experiment [31]. No-slip boundary conditions are applied at both upper, lower, and two sided planes to better describe the model physically and mathematically.

SIMPLE (Semi-Implicit Method for Pressure-Linked Equations) algorithm is applied both here and in the transport model to calculate the pressure and velocity fields at each time step. It firstly calculate the intermediate velocity from discretizing momentum equation. Then solve the pressure and apply under-relaxation. The next step is correct the mass fluxes calculated before the pressure, and then correct the velocity based on the new pressure and update the boundary conditions. These steps are repeated until convergence criteria has been met [49].

2.2.2 Reactive transport

The steady-state advection-diffusion reaction equation is solved using the velocity field from the results of the first step of the model. We assume that the precipitation reaction at the lower plate is kinetically controlled [57], [33]. The precipitation reaction happens at the seeded places represented by the reactive patches in the model. The governing equation of the reactive transport module is given by:

$$\nabla \cdot (\vec{U}C) - \nabla^2(D_T C) = 0 \tag{2.3}$$

where D_T is the molecular diffusion coefficient and is set to be 1×10^{-12} (m^2/s) based on the properties of the fluid.

A dimensionless concentration, $\hat{C}$, is introduced here for the simplification of the developed

boundary condition which will be discussed later.

$$\hat{C} = \frac{C_S - C}{C_S} \tag{2.4}$$

Gradient scheme for transport module is same as the flow field solver. Two divergence schemes are used to get a comprehensive understanding of both the schemes and the model. One is *bounded Gauss limitedLinear* for scalarTransportFoam. *limitedLinear* is an interpolation scheme that limits towards *upwind* scheme when the gradient is large [60].

The other divergence scheme is *bounded Gauss upwind* for scalarTransportFoam. *Upwind* scheme is first-order accurate in both time and space as mentioned in last section, and is always bounded. However, upwind scheme is known as introducing serious numerical diffusion to where gradients are large in two- or three-dimensional coordinate systems. Perverse results will also be produced by the scheme when the flow direction is not aligned with the grid centerlines [64]. Numerical diffusion is also called false diffusion somewhere, and is raised from a first-order difference approximation to the spatial derivative $\partial u/\partial x$. Using higher-order accuracy finite difference approximations, like central difference approximation with second-order accuracy, can eliminate this diffusion like problem that underestimates the gradient in the system [62]. Nonetheless, when the Peclet number of a grid cell is larger than 2, higher-order finite difference approximations are usually unstable, and thus upwind scheme is back into sight. The numerical diffusion acts as a stabilizing factor on the solution, and it is also the reason of producing inaccurate results.

Laplacian scheme is *Gauss linear corrected* for both solvers, and it is an unbounded, second-order, conservative scheme.

Fixed concentration boundary condition is imposed at the inlet, while zero gradient concentration boundary condition is imposed at the outlet, and both upper and lower plates except for the reactive patches. Cyclic boundary conditions are again applied to the two

sided faces. A boundary condition was developed specifically for the precipitation reaction of calcium carbonate at reactive patches, which corresponding to the seeded sites in the experiment, on the lower plate.

$$D_T \nabla \hat{C} = -k\hat{C} \tag{2.5}$$

$$\hat{C}_b = \frac{D_T}{k\delta + D_T}\hat{C} \tag{2.6}$$

where k is the precipitation rate, and δ is the grid size.

Inflow concentration is fixed at 1 (mol/m^3) at inlet ($x = 0$ mm), and zero gradient boundary conditions, $\partial C/\partial x = 0$, are applied at all the rest boundary faces including outlet, upper wall, lower wall and two sided walls.

2.3 Two-dimensional flow and reactive transport model

2.3.1 Velocity field

As introduced in section 1.2.4, the two-dimensional flow and reactive transport model developed in previous study [11] is not simply integrating in the third dimension.

A depth-averaged flow field is calculated from the three-dimensional Stokes equations

$$\frac{\partial b}{\partial t} + \nabla \cdot \boldsymbol{q} = 0 \tag{2.7}$$

$$\boldsymbol{q} = -\frac{b^3 g}{12\nu}\nabla h \tag{2.8}$$

b is the local aperture, ν is the kinematic viscosity, and h is the hydraulic head.

2.3.2 Reactive transport

Transport equation is also depth-averaged and includes dissolution reactions.

$$\frac{\partial(bc)}{\partial t} + \nabla \cdot (\boldsymbol{q}c) - \nabla \cdot (b\boldsymbol{D}\nabla c) = R(c) \tag{2.9}$$

$\boldsymbol{D}$ is a local dispersion tensor, and is equal to molecular diffusion coefficient here due to negligible value of Tyler dispersion in this study. $R(c)$ is the effective local reaction rate.

The change of local aperture is updated at the end of each iteration as the quasi steady state is reached. Dissolution reaction rate is regulated by the advection-diffusion transport and the kinetics of chemical reactions occurring at the surface, and is modeled by integrating effective mass transfer and reactive kinetics here.

Some modifications have been applied to make this fracture dissolution model become a mineral precipitation reactive transport model, and compare with the three-dimensional model developed in this thesis. Since the three-dimensional model does not account for the change of aperture during the precipitation process, $\partial b/\partial t$ in the equations above is set to be zero. Equilibrium concentration, C_s, is set to be 0, which is smaller than c, and thus the reaction rate $R(c)$ is negative, indicating the removal of solutes from the flow system.

For both the two- and three-dimensional models, the same variables were studied, which include the aperture field, as well as the pressure gradient. Model parameters and con-

stants are set to be the same for both models, like geometry size, diffusion coefficient, inflow concentration, equilibrium concentration, and etc.

2.4 Model domain, boundary conditions and meshing

The model domain is 150 mm × 150 mm × 0.15 mm (width × length × height) with a smooth plane as the lower plate, and a rough surface as the upper plate as shown illustratively in Figure 2.1 (b). The rough surface is modified from the measurements from a real glass plate by reducing the standard deviation of the aperture to produce a smoother surface. The standard deviation to mean ratio, $\sigma/\bar{b}$, is 0.3 for the measured aperture field. Several parameters, including resolution in aperture height direction, aperture fields, and relative roughness of fracture surfaces, are modified to assess sources of errors and to test the soundness of the model. An extreme case with the roughness of fractured plate reduced to zero, i.e. the rough surface becomes a smooth surface is also performed. This is to validate the three-dimensional model by comparing with analytical solution, as well as to evaluate the influence of roughness on calculated results. The domain is oriented so that positive y direction corresponds with the flow direction.

The model is made up of two components: a flow module, and a reactive transport module. It is assumed that the flow field is at steady-state as an input into the transport module, and remains at steady-state as the concentration field develops with time. No slip boundary condition are prescribed for the top, bottom and two sided plates. The pressure gradient between inlet and outlet is same as the actual model, which is 30 (Pa). The top and bottom plates of the test model are set to be reactive with an infinite reactive rates, in other words, concentration of solute is zero at the two plates. A boundary condition was modified using a library named groovyBC in swak4Foam specifically for precipitation of calcium carbonate at reactive sites on the lower plate. Figure 2.1(a) indicates the location of reactive patches.

The most frequently used mesh shape is hexahedron mesh, i.e. block mesh in OpenFOAM. Modified hexahedron mesh is used in this model due to different height of aperture at each grid caused by the rough top plate. The width and length of each cell is uniform and has a value of 1 (mm) in both direction, while the height of cells differ from each other. At a given x and y coordinate, there is a fixed aperture height, and since the number of grids along z direction is also fixed (number of grids in z direction, $n_z = 12$), the height of each grid is therefore calculated and assigned. Since the top plate is a rough surface, as illustrated in Figure 2.2, all the mesh blocks have corner points that cannot form either top or bottom face as a plane. However, the points can still form four sided faces for each block as the increments in x and y directions are uniform. Red arrow indicates cell$'s$ center-to-center direction, while the black arrow represents the direction of flux calculated in OpenFOAM. Thus, the non-orthogonality of the mesh grids needs to be taken into consideration to count in the error brought by the inconsistency between the direction of flow and grid centerline. Flow in z direction might include error comes from the inclined top and bottom faces. An non-orthogonal corrector factor known as nNonOrthogonalCorrectors is added to the SIMPLE algorithm. The nNonOrthogonalCorrectors is used widely in all kinds of solvers and applications. It defines the number of iterations pressure equation needs to go through before the convergence criteria has been met within each time step, and also is responsible for updating the explicit non-orthogonal correction[60].

Due to the properties of OpenFOAM, the model domain is divided into $150 \times 150 \times 1$ sub-domains, where the bottom face of each one subdomain can be treated as one reactive patch that the developed precipitating boundary condition can be applied to. The coordinates of reactive patches are assigned by the measured calcium carbonate seeds sites from Jones experiment. Overall, there are $150 \times 150 \times 12$ mesh grids in the domain, with the size of each grid equals to 1 mm$\times$ 1 mm$\times$ (approximately) 0.01 mm.

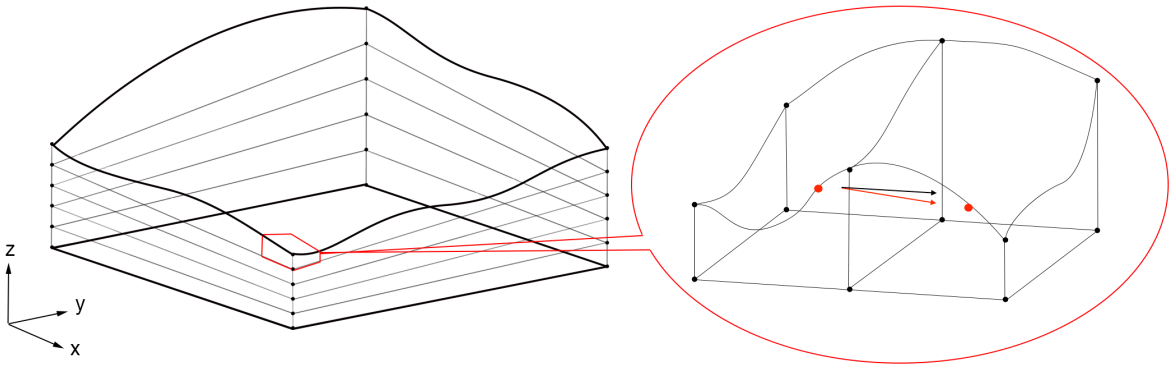

Figure 2.2: Illustration of the non-orthogonality of the mesh. The red arrow indicates cell′s center-to-center direction, while the black arrow represents the direction of flux calculated in OpenFOAM.

Chapter 3

Results and Discussion

This section presents results from simulationsusing the model presented in Chapter 2. The presentation of the results is organized as follows: computed velocity and transport fields for variable-aperture fractures, both smooth-walled case and tough-walled case; computed velocity fields for cases with (i) different resolutions in aperture height; (ii) different fracture fields; (iii) different relative roughness ($\sigma/\bar{b}$) of fracture; and comparison of computed velocity and transport fields between three-dimensional model developed in this thesis and two-dimensional model from previous studies.

3.1 Velocity field

3.1.1 Parallel-plate fracture

After running the first step of the parallel-plate model, a flow continuity test is conducted with the computed results in order to check the mass conservation within the domain. Flow rates across each mesh grid block face is calculated by multiplying the velocity by the area

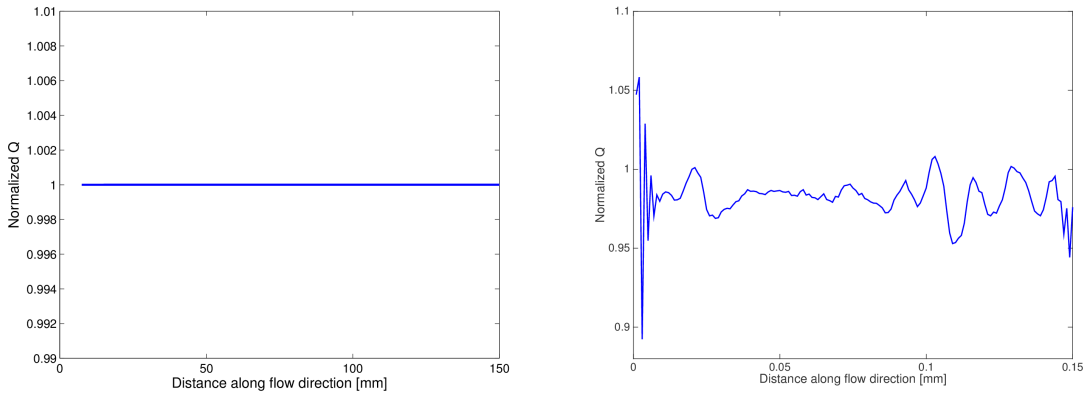

Figure 3.1: (a) Flow continuity test for parallel plate model. The horizontal straight line indicates a perfect conservation of mass. (b) Flow continuity test for the rough-walled model with $\sigma/\bar{b}$=0.3 (case 1). Significant fluctuations at both inlet and outlet reflect mass conservation errors that are likely due to nonorthogonality of the mesh, which increase with $\sigma/\bar{b}$.

of the face. Summing up flow rates across $x-z$ planes at different locations (y) along the flow direction provides a test of mass conservation (Figure 3.1(a)). The horizontal line of flow suggests theres no mass change in the direction of flow, implying flow is well-conserved. Actually, all the points with same z coordinate have same velocity profile since it is a parallel plates system. The analytical solution is derived below and used to plot with the comparison between the modeled data. Figure 3.2(a) shows the velocity profile across the fracture aperture at a random point ($x = 98$ mm, $y = 60$ mm) in the fracture plane, and the analytical solution at the same point.

$$u = \frac{3}{2} \times \bar{u} \times [1 - (\frac{z}{H})^2] \tag{3.1}$$

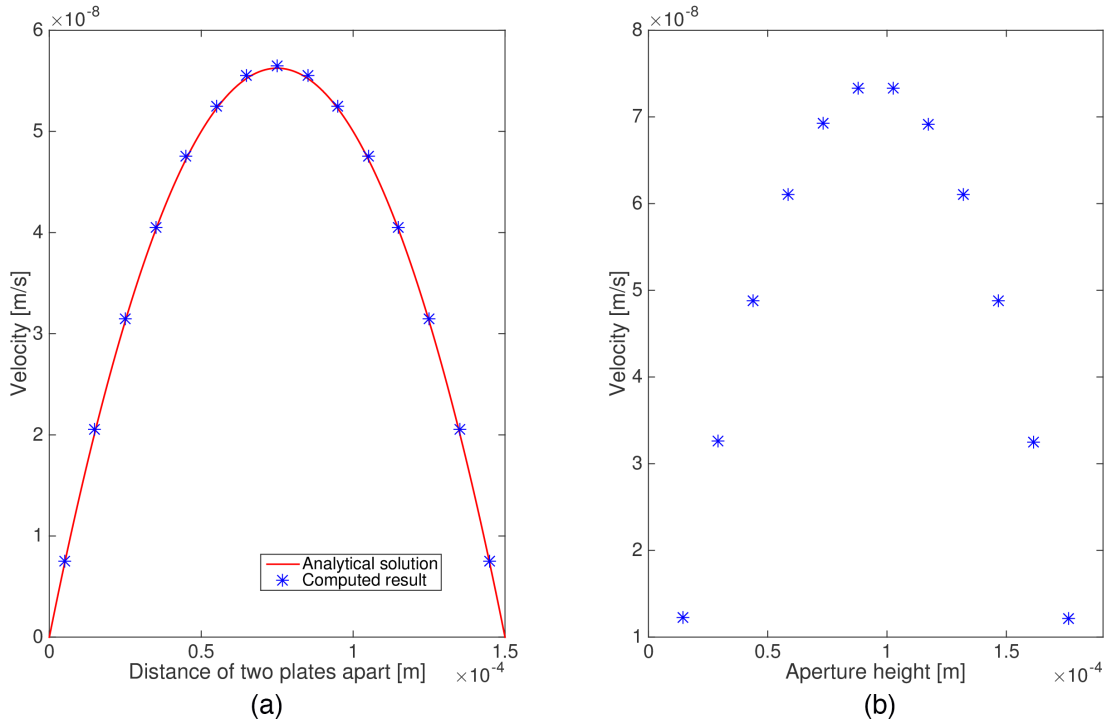

Figure 3.2: (a) Blue asterisks are computed results at (x = 98 mm, y = 60 mm) for the smooth-walled model, and the red curve is analytical solution of parallel plate flow. (b) Velocity profile from the rough-walled model with $\sigma/\bar{b}$=0.3 at the same location (x = 98 mm, y = 60 mm).

$$\bar{u} = -\frac{H^2}{3\mu} \times \frac{dp}{dx} \tag{3.2}$$

H is half of the distance between two parallel plates, μ is the dynamic viscocity, $\bar{u}$ is the mean velocity.

The parabolic shape of the velocity profile and high goodness of fit between the computed result and the analytical solution confirms the validity of the model, and supports applying the model to variable-aperture fracture.

3.1.2 Rough-walled fracture

Here we simulate the velocity field in a variable-aperture fracture (case 1). The original case is an aperture field measured by Jones and Detwiler for a real rough glass plate, with a mean of 0.147 (mm) and a standard deviation of 0.044 (mm). The ratio between standard deviation and mean is therefore equals to $\sigma/\bar{b} = 0.3$. This parameter defines the relative roughness of the fracture, with larger values indicating a rougher fracture surface, while smaller ratio reflects smoother surface. Surfaces with different $\sigma/\bar{b}$ ratio will be analyzed and compared in the following section. Figure 3.1(b) shows results from the same continuity test performed for the parallel plate test. Fluctuations are observed near both inlet and outlet, while in the middle of the flow field mass conservation is improved. The discontinuity will be taken into account for future errors.

Matlab is then used to load and process results of all the simulations. The list of result is firstly constructed into a $150 \times 150 \times 12$ matrix, then summed over z direction, multiplied by the aperture height and grid width element-by-element. Now the flow field is ready to be plotted in two-dimensional images.

$$\bar{Q_y} = \sum_{n=1}^{12} U_{i,j,n}|_y \times b_{i,j} \times \delta \tag{3.3}$$

Figure 3.2 (b) is a velocity profile at the same location as Figure 3.2 (a), and still remains a parabolic shape, although the magnitude is different, fractured model has smaller maximum and mean velocity. There might be three major reasons for this decrements. While one is head loss due to roughness of the fracture; another reason might be the local aperture height is 0.191 (mm), which is higher than the height of parallel plate (0.15 mm), thus resulting in a gentler local flow profile at the point ($x = 98$ mm, $y = 60$ mm); the last one could be the division of velocity into other directions for the aperture field computation, and there was almost no flow in the two dimensions other than the flow direction for the test model. The

mean flow rate in the flow direction is 3.02×10^{-8} (m/s), smaller than 2.75×10^{-8} (m/s), which is the mean of analytical flow rate for the parallel plate system.

3.1.3 Analysis of the impact of different properties of the model on the result

Different resolutions in aperture height direction

Five simulations (case 2 to 6) each with a different number of grid blocks along z direction (n_z =1, 5, 10, 12, 15) systematically test the influence of resolution in the z-direction on the computed results. Depth-averaged flow rate across cross-sectional face perpendicular to the direction of flow is plotted in Figure 3.3 for each of the different resolution. A two-dimensional flow test is also conducted with the same fracture field in order to provide a reference curve, and is plotted on Figure 3.3 as well. As indicated in the plot, there is no obvious difference between different grid resolutions. For some schemes in finite volume method, errors of the output can be proportional to the aspect ratio [12], which is the ratio of the width to the height of a grid. It is also reported that when running with parallel incompressible CFD algorithms, the convergence rate will decrease greatly if decomposing the domain along a direction with high aspect ratio [29]. The maximum aspect ratio ranges from 6.03 to 120 for these five simulations, while all the meshes pass the screening test performed by checkMesh, a utility in the OpenFOAM toolbox that checks the validity of a mesh.

SimpleFoam uses a Gauss-Seidel scheme for solving the resulting system, which is the smoother of equations. This scheme becomes unconditionally stable at low Reynolds numbers [4]. Reynolds number in our model is around 2×10^{-5}, which is extremely small. This outcome excludes the influence of aspect ratio on the discontinuity of the computed flow field. $n_z = 12$ is then selected as the constant number of grids along z direction as a balance

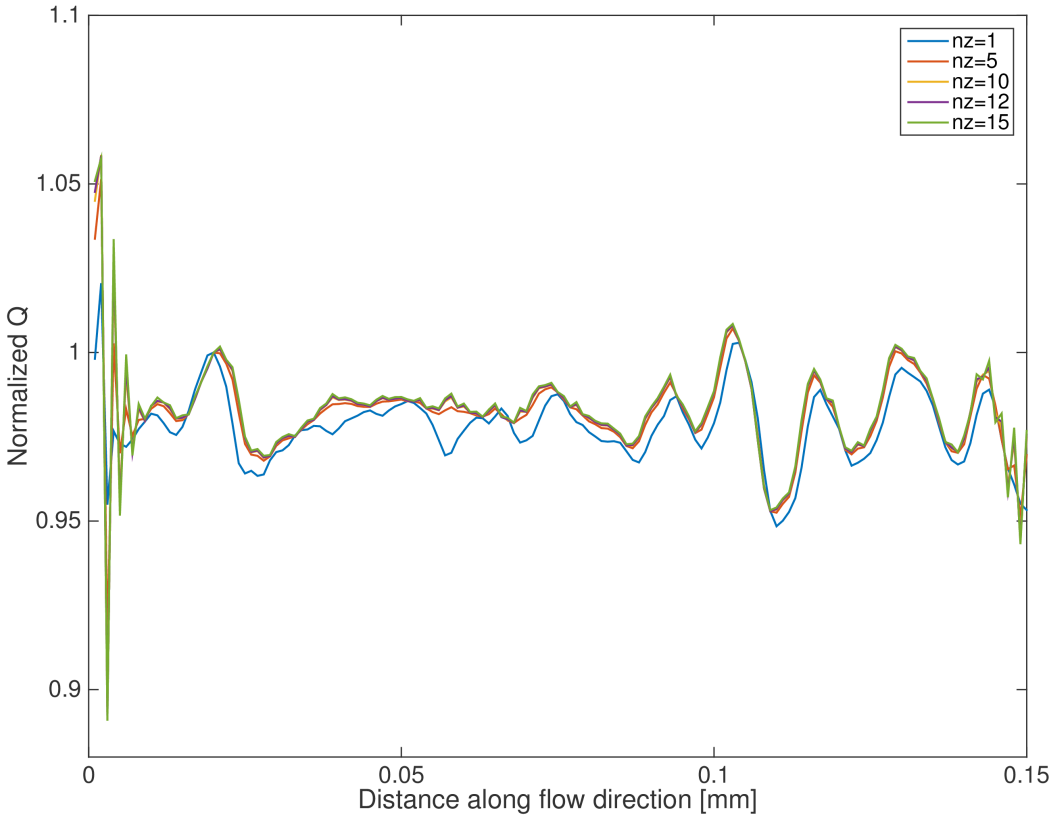

Figure 3.3: Flow continuity test results for five simulations with different number of grids in z direction as incated on the legend located at top right of the plot. Five curves has similar trends, while the blue curve that represents $n_{\times}z$=1 is the most discrepant one from other four.

between the accuracy and efficiency.

Different aperture fields

Flow is simulated through three different aperture fields to test the influence of relative roughness on the flow fields. These three fields are subsets of the measured data of a piece of real glass, which has a size of 1786×1779, and they all have a size of 100×100. The outcomes of three cases are shown in Figure 3.4, warmer color refers to higher flow rate, and cooler colored regions endure lower rates. A few stripes near both inlet and outlet are

observed, which correspond to oscillations of velocity along the flow direction in previous continuity test(Figure 3.1). Case number 8 shows the least persistence of the oscillations, and the largest aperture (0.185 mm) at the inlet. The other two cases have similar means of aperture height, but case 10 has lower inlet aperture (0.121 mm comparing to 0.142 mm for case 9), thus results in more stripes than case 9. These results suggest that a larger mean aperture at the inlet leads to fewer localized errors in the velocity field. Flow in aperture with larger mean value is more fairly distributed in the field like case 8, and is more channelized in fields with lower mean value, like case 9 and 10. Flow of case 10 is centralized in one channel indicated by the deep red tube in Figure 3.4. The stripes embody the distorted calculated results, many different methods and ways of computation have been applied, but none of completely remove the existence of the oscillations in the velocity field.

Different $\sigma/\bar{b}$ ratio using synthetic fracture fields

Aperture heterogeneity also impacts the accuracy of the computed flow field. Three synthetic fracture fields with $\sigma/\bar{b}$ ratio = 0.02, 0.05, and 0.1 are generated by modifying the $\sigma/\bar{b}$ ratio of the original aperture field in case 1. The flow continuity test is again carried out for the three simulations, and Figure 3.5 shows the mass conservation within each models system, with the black curve of original field (case 1) as reference. When $\sigma/\bar{b}$ ratio is 0.02, which is the blue curve on the plot, normalized flow is almost a horizontal line with fluctuations that are less than 0.5%. Nonetheless, the reference black curve with a $\sigma/\bar{b}$ ratio = 0.3 is strongly oscillating along the flow direction, especially, near the inlet and outlet.

The curves reflect several trends. One is that the accuracy of the computed flow is inversely proportional to the roughness of aperture, as the curve of $\sigma/\bar{b}$ ratio = 0.02 is much more gradual than the curve of $\sigma/\bar{b} = 0.1$. The other is the fluctuation of mass conservation has correlation with the apertures undulation. Although with different magnitude, the general shape of the averaged flow curves among three simulations have remained the same. Since

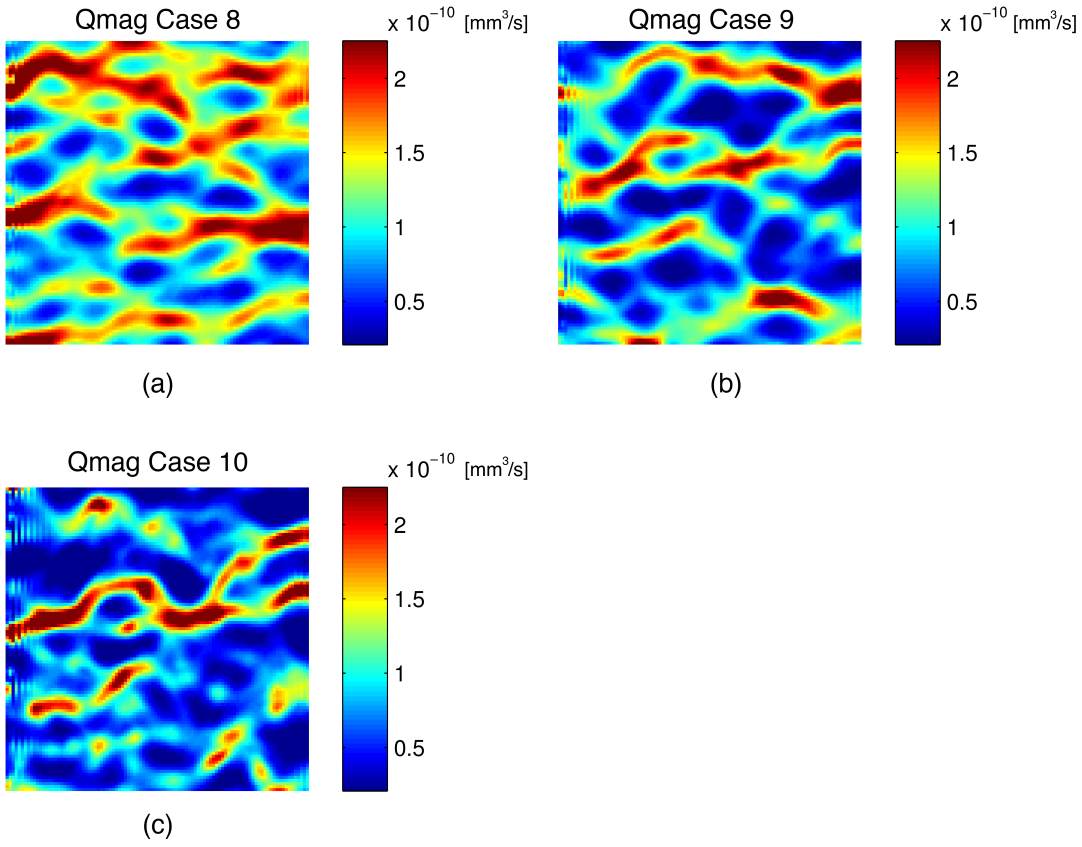

Figure 3.4: (a) Magnitude of flow for case 8. The magnitude is calculated with the depth-averaged velocity in the flow direction (y) and x direction. (b) Magnitude of flow for case 9. (c) Magnitude of flow for case 10. It is the most channelized flow field among the three cases, however, the width of striped bands is also the widest.

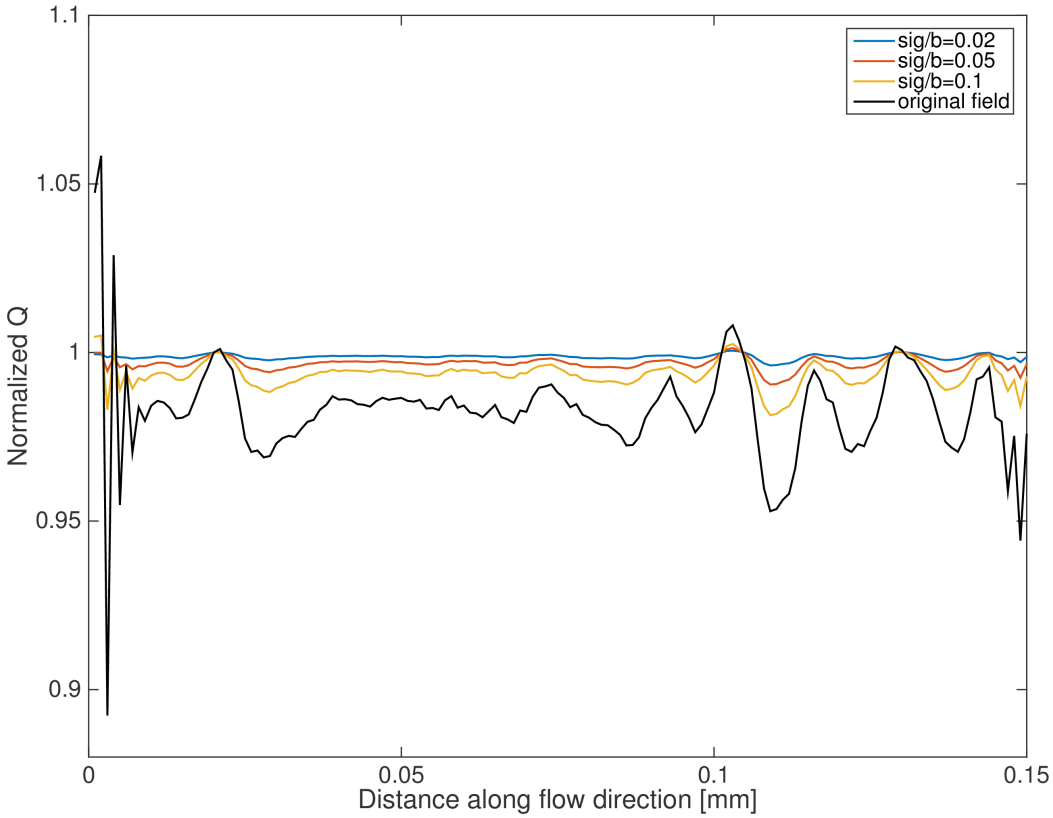

Figure 3.5: Flow continuity test results for three synthetic fields with $\sigma/\bar{b}$ ratio = 0.02, 0.05, and 0.1. Black curve is the test result of case 1, which has a $\sigma/\bar{b}$ ratio od 0.3. These curves show that the smaller the value of $\sigma/\bar{b}$ ratio is, the better the mass conservation is within the model domain.

the parallel plate test case showed perfect conservation of mass in Figure 3.1, it is surmisable that with the smoothening of fractured plate, the magnitude of errors decrease to approach zero for the smooth case. In a previous study of three-dimensional simulation of fracture dissolution with OpenFOAM, researchers limited their study to $\sigma/\bar{b} = 0.01$ [56]to avoid errors induced by high-aspec, non-orthogonal grid blocks. The results presented here are consistent with limiting simulations to such small values of $\sigma/\bar{b}$.

3.1.4 Comparison with two-dimensional model

Figure 3.6 shows a comparison of depth-averaged three-dimensional flow field calculated from the model built in this thesis with a two-dimensional simulation of flow in fracture with the same aperture field and boundary conditions. The aperture used here is identical to the one in case 1. Few differences can be observed from (a) and (b), besides the stripes near inlet and outlet of the three-dimensional model. The two models both capture the major channel at the lower part of the aperture, where the highest flow rate is around 14×10^{-3} (mm^3/s). They also predict the same minor channels as the regions with warm color in the plot demonstrate. Figure 3.6(c) shows a plot of the percent difference between two models using the flow field from the two-dimensional model. As we expect, the average difference is within 0.02%, except for the area near both inlet and outlet where the previous-discussed velocity oscillations are observed for the three-dimensional case. Since the difference is flow rates of three-dimensional model subtracted from flow rates of two-dimensional model, and the middle region of Figure 3.6(c) is slightly above zero, a deduction that the two-dimensional model produces slightly higher flow rates in most locations within the model domain. Dark blue regions near inlet suggest higher flow rates of three-dimensional model have have taken place here, but this region is subject to spurious velocity oscillations and likely not accurate.

3.2 Reactive transport

3.2.1 Parallel-plate fracture

The three-dimensional calculated velocity field is used as input for the transport model. Figure 3.7 is the weighted concentration profile by velocity along the flow direction and averaged over both depth and width of the model to produce a set of processed one-dimensional data

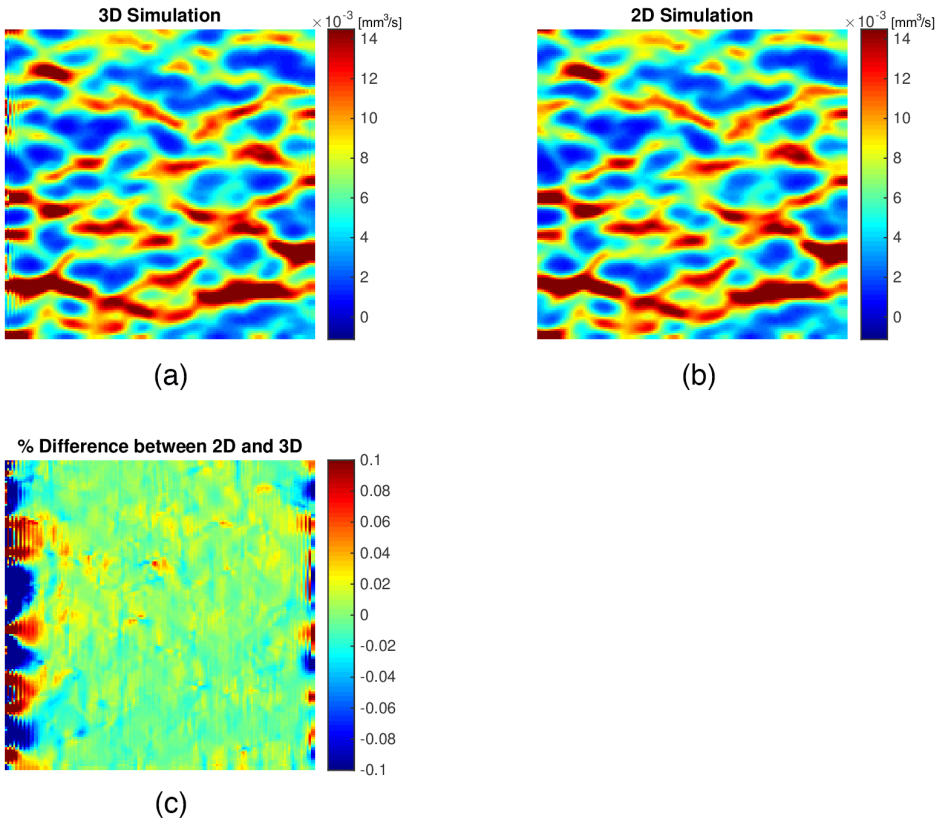

Figure 3.6: Comparison between velocity field from three-dimensional model (a), and from two-dimensional model (b). (c) is a plot of percent difference between these two models.

in order to compare with the fitted equation, which is the solid curve with coefficient of determination, R^2 equals to 0.999. The fitted curve has an exponential shape as the following equation.

$$C = A \times e^{-Bx} = 0.9314 \times e^{-9.178x} \tag{3.4}$$

Effective reaction rates, k_{eff} (mm/s), are computed for both modeled result and analytical solution to evaluate the accuracy of the three-dimensional model.

For the three-dimensional model,

$$k_{\text{eff,mod}} = B \times \bar{u} \times b = 5.16 \times 10^{-5} \tag{3.5}$$

where B is the fitted parameter obtained from Equation 3.4, $\bar{u}$ is the mean velocity, and b is the distance between two parallel plates.

For the analytical solution,

$$k_{\text{eff,ana}} = \frac{2k}{1 + Da'} \tag{3.6}$$

where k is the reaction rate, Da' is a modified local Damkohler number

$$Da' = \frac{2kb}{ShD_T} \tag{3.7}$$

The dimensionless Sherwood number, Sh, is 7.56 according to Kay [34]. Since a spontaneous reaction is applied at both top and bottom surfaces, k is equal to infinite. And Equation 3.6 has become

$$k_{\text{eff,ana}} = \frac{ShD_T}{b} = 5.04 \times 10^{-5} \tag{3.8}$$

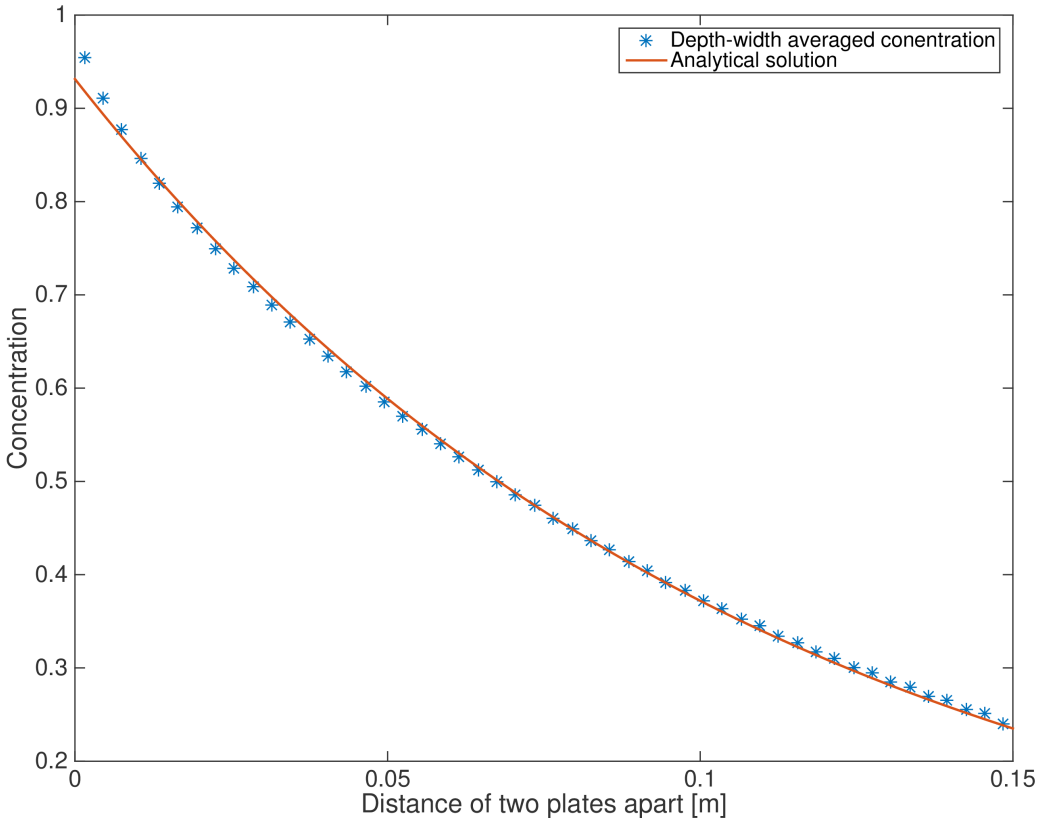

Figure 3.7: 1-D concentration profile (blue asterisks) calculated by averaging along x direction and then flux-weighted over z direction with fitted exponential curve.

The little difference between $k_{\text{eff,mod}}$ and $k_{\text{eff,ana}}$ and high correlation between the computed concentration and fitted curve in Figure 3.7 , confirm the validity of the transport model, and builds confidence in applying model to variable-aperture fractures.

There is a slight discrepancy between the two curves near the inlet. This is very likely due to the development length, or entry length. The reason for the existence of development length is that the analytical solution presumes a fully-developed concentration field; that is one in which the dimensionless concentration does not change in the flow direction. However, the concentration is uniform at the inlet, and requires some distance to become fully-developed. Up to this point, the validation of the transport model has been completed, and the model is ready to perform more complicated simulations.

3.2.2 Rough-walled fracture

After running case 1, a list of results of concentration at the center of each grid block has been produced. Matlab is again used for post-processing. Depth-averaged concentration is produced by summing up the concentration at each grid center along the aperture direction, and then divided by the number of grid blocks in z direction.

$$\bar{C}_{i,j} = \frac{1}{n_z} \sum_{n=1}^{n_z} C_{i,j,n} \tag{3.9}$$

Figure 3.8(a) shows $\bar{C}$ in the aperture field. Bright colored spots correspond to the locations of calcite seeds on the lower plate. Flow of calcium and carbonate ions is depleted when passing these sites due to the precipitation reaction. Thus an overall decrease of concentration level can be observed along the flow direction. A comparison view of computed concentration field with *upwind* and *limitedLinear* schemes is shown in Figure 3.8. It is clear that the *upwind* scheme produces a more diffusive field with blurred flow tubes, but concentration within the domain is bounded. The result of *limitedLinear* scheme is unbounded (concentration exceeds 1 near inlet), while 5 distinct channels indicate reduction of false diffusion. It is also worth noting that the stripes near the inlet and outlet for the flow field are smeared by *upwind* scheme, while staying in situ with the *limitedLinear* scheme.

The *limitedLinear* scheme acts as *upwind* scheme where the change of gradient is rapid to avoid unstable result, otherwise, a second-ordered *linear* scheme will be applied. A coefficient is required when setting up the model with this scheme. One can pick any number in between 0 and 1. 1 is strongest limiting, and 0 is weakest. However in our model, *limitedLinear* scheme didn′t manage to bound the results. In regions with lower gradient, the higher-order scheme is turned on, and produces results with more details. The five apparent flow paths are the best verification. Notice that the second-ordered *linear* is unbounded, and may be responsible for the overshoot of concentration near inlet where the gradient is extremely

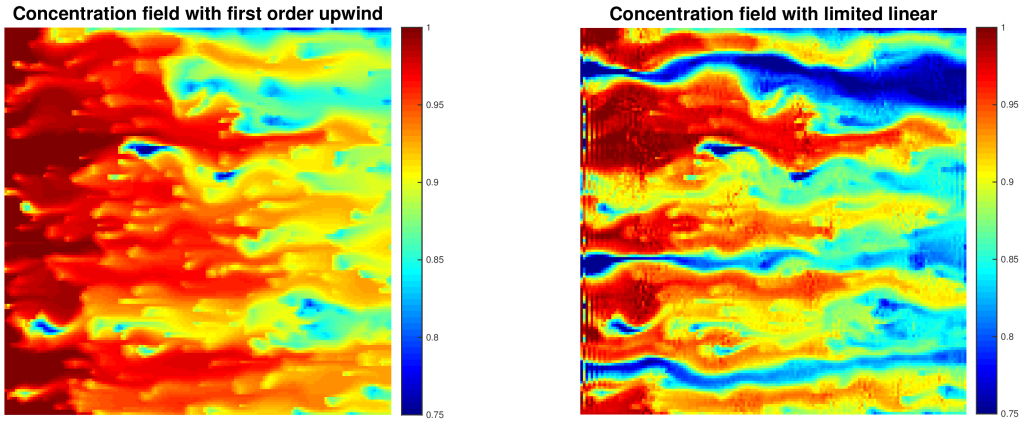

(a) (b)

Figure 3.8: (a) Depth-averaged concentration field using first order upwind scheme. (b) Normalized depth-averaged concentration field using higher order limited linear scheme.

steep.

The *upwind* scheme is no stranger to most people, since it is a really simple yet useful scheme under many circumstances. The wide spread red regions in the plotted depth-averaged concentration field Figure 3.8(a) is an artifect of the effect of false diffusion. Years of efforts have been made to develop or modify an easy-to-use yet affordable scheme without false diffusion that is still bounded and stable, however, none is as easily applicable as the *upwind*. Many numerical methods have been developed to solve complicated equations over decades, false diffusion remains a knotty problem. In this thesis, the *upwind* scheme makes a good performance dealing with disordered gradients, and the false diffusion problem is acceptable with the current level of study. Therefore, we choose *upwind* scheme as the divergence scheme in all the simulations that are going to be displayed.

3.2.3 Comparison with two-dimensional model

Figure 3.9 shows a comparison of a depth-averaged concentration field at steady state from the three-dimensional model and a steady-state concentration field calculated from the two-dimensional model from previous study [11]. Since first-order upwind scheme is chosen as the divergence scheme in the three-dimensional model, the high-ordered upwind scheme used in the two-dimensional model is replaced by first-order upwind for this study. Boundary conditions and model parameters remain the same for both models.

These two plots follow a same general pattern. They have similar fingers of concentration, and have warm and cool colored regions that are little different from each other. The mean difference between the computed results from these two models 2.15×10^{-4} mol/m^3, while the maximum difference occurs midway along the x direction near the inlet with a value of 0.17. The difference of averaged concentration at the outlet between the two models is less than 0.005, which discloses that the results of transport model from the two computational models are at a high degree of uniformity.

Notwithstanding, there do exist some differences. First of all, regions with cooler color are defined clearer in two-dimensional model. This indicates a steeper gradient of concentration is provided by the two-dimensional model by showing distinct edges of flow fingers. While the margin of concentration flow in the three-dimensional model is blurry. Secondly, there are much more yellow spots in three-dimensional model than in two-dimensional model. These yellow spots correspond to the locations of calcite seeds, where the precipitation process takes place. They are surrounded by orange and red regions, signifying the consumption of solutes at these locations, and further proving their identity as the reactive sites. This information is missed in the two-dimensional model.

This discrepency is likely due to the fact that the two-dimensional model presumes a fully-developed concentration field at each reaction site. Because the three-dimensional model

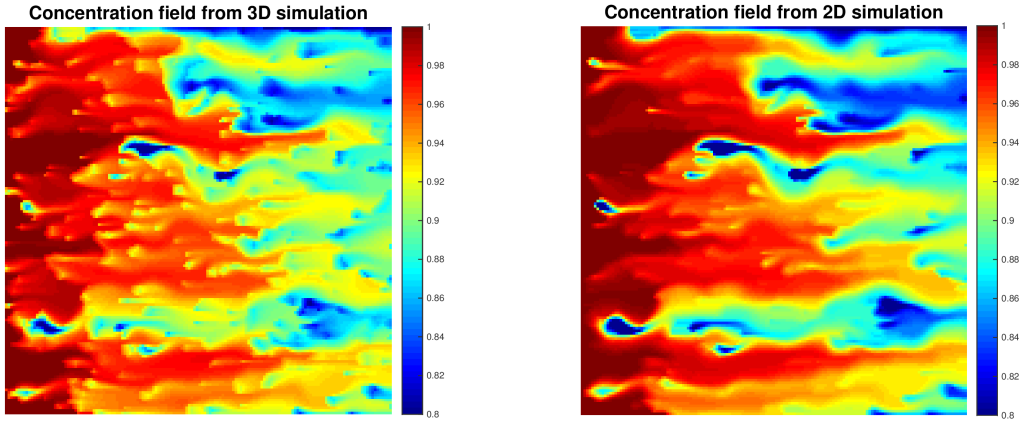

(a) (b)

Figure 3.9: (a) Concentration field from three-dimensional model (b) Concentration field from three-dimensional model

makes no such assumption reaction rates tend to be higher in the three-dimensional model (e.g. see the discrepency between the analytical and simulated concentration for the parallel-plate case Figure 3.7).

Chapter 4

Conclusions

In this thesis, OpenFOAM, an open source CFD toolbox is modified to deal with modeling of three-dimensional mineral precipitation process in fractured media. The two-step model is developed with the help of simplFoam and a modified version of scarlarTransportFoam, both of which are built-in standard solvers in OpenFOAM.

A parallel plate test model is firstly set up with boundary conditions similar to the rough-walled model. Continuity tests are run for computed flow field and transport field. The encouraging results from the tests suggested the three-dimensional model is greatly set up.

Three parameters were evaluated to explore sources of errors and build confidence in the model. Tests with different resolutions across the fracture aperture excluded the influence of aspect ratio on the discontinuity of the computed flow field; results from apertures with different height brought the possibility of linking the distorted stripes of abnormal flow rates with the average height of aperture; synthetic fields with different $\sigma/\bar{b}$ ratio show that the larger the ratio is, the more significant the fluctuation of error will be.

Comparing the results of both the flow field and the transport field from the newly-built

three-dimensional model with the results from the two-dimensional model show similar results with some potentially important discrepancies. These include: (i) discrepancies in the magnitude of the flow rate for the same pressure gradient; and (ii) discrepancies in reaction rates and local concentrations at reaction sites. One of the advantages of the model is the details of transport field showing in the results. However, it takes less than 10 seconds to run a two-dimensional model, while 5 hour to run a three-dimensional model with the mesh size mentioned in Chapter 2.

Future study can be focused on improving the outcome of flow field to eliminate stripes near both inlet and outlet, and the updating of geometry changes due to the precipitation process.

Bibliography

[1] Atkinson, T. C. *Carbon dioxide in the atmosphere of the unsaturated zone: an important control of groundwater hardness in limestones* Journal of Hydrology, 1977, 35(1-2), 111-123.

[2] Bachu, S., Gunter, W. D. Perkins, E. H. *Aquifer disposal of CO2: hydrodynamic and mineral trapping* Energ. Convers. Manage., 1994, 35, 269279.

[3] Brodland, G. W. *How computational models can help unlock biological systems.* In Seminars in cell and developmental biology, 2015, Vol. 47, pp. 62-73. Academic Press.

[4] Buelow, P. E. O., Venkateswaran, S., and Merkle, C. L. *Effect of grid aspect ratio on convergence.* AIAA journal, 1994, 32(12), 2401-2408.

[5] Carbonate mineral *In Encyclopaedia Britannica Online.* 1998, Retrieved from http://www.britannica.com

[6] Chakrabarty D, Mahapatra S. *Aragonite crystals with unconventional morphologies* J Mater Chem. 1999, 9:29532957.

[7] Chaudhuri, A., H. Rajaram, and H. Viswanathan *Alteration of fractures by precipitation and dissolution in gradient reaction environments: Computational results and stochastic analysis* Water Resources Research, 2008, 44(10), W10,410.

[8] Chernov, A. A. *The spiral growth of crystals* Physics-Uspekhi, 1961, 4(1), 116-148.

[9] Chernov, A. A. *Formation of crystals in solutions.* Contemporary Physics, 1989, 30(4), 251-276.

[10] De Yoreo, J. J., Vekilov, P. G. *Principles of crystal nucleation and growth* Reviews in mineralogy and geochemistry, 2003, 54(1), 57-93.

[11] Detwiler, R. L., and Rajaram, H. *Predicting dissolution patterns in variable aperture fractures: Evaluation of an enhanced depthaveraged computational model.* Water resources research, 2007, 43(4).

[12] Diskin, B., and Thomas, J. L. *Effects of Mesh Irregularities on Accuracy of Finite-Volume Discretization Schemes* 2012

[13] Dreybrodt, W., Eisenlohr, L., Madry, B., Ringer, S. *Precipitation kinetics of calcite in the system CaCO3-H2O-C02: The conversion to CO2 by the slow process H++ HCO3¿ CO2+ H2O as a rate limiting step* Geochimica et Cosmochimica Acta, 1997, 61(18), 3897-3904.

[14] Druhan, J. L., Steefel, C. I., Williams, K. H., and DePaolo, D. J. *Calcium isotope fractionation in groundwater: Molecular scale processes influencing field scale behavior* Geochimica et Cosmochimica Acta, 2013, 119, 93-116.

[15] Earle, S. *Groundwater geochemistry* Retrieved from Vancouver Island University Hydrogeology site.

[16] Erwee, M. W., Reynolds, Q. G., and Zietsman, J. H. *Comparison of 2D and 3D Computational Multiphase Fluid Flow Models of Oxygen Lancing of Pyrometallurgical Furnace Tap-Holes* JOM, 2016, 68(6), 1556-1562.

[17] Evans, M. W., Harlow, F. H., and Bromberg, E. *The particle-in-cell method for hydrodynamic calculations* (No. LA-2139)., 1957, LOS ALAMOS NATIONAL LAB NM.

[18] Fallah, N. A., Bailey, C., Cross, M., and Taylor, G. A. *Comparison of finite element and finite volume methods application in geometrically nonlinear stress analysis.* Applied Mathematical Modelling, 2000, 24(7), 439-455.

[19] Ferris, F. G., Phoenix, V., Fujita, Y., Smith, R. W. *Kinetics of calcite precipitation induced by ureolytic bacteria at 10 to 20 C in artificial groundwater* Geochimica et Cosmochimica Acta, 2004, 68(8), 1701-1710.

[20] Fujita, Y., J. L. Taylor, T. L. T. Gresham, M. E. Delwiche, F. S. Colwell, T. L. McLing, L. M. Petzke, and R. W. Smith *Stimulation of microbial urea hydrolysis in groundwater to enhance calcite precipitation* Environmental Science and Technology, 2008, 42(8), 30253032.

[21] Gehrke, N., Clfen, H., Pinna, N., Antonietti, M., and Nassif, N. *Superstructures of calcium carbonate crystals by oriented attachment.* Crystal Growth and Design, 2005 5(4), 1317-1319.

[22] Goodarz-nia, I. and Motamedi, M. *Kinetics of Calcium Carbonate Crystallization from Aqueous Solutions* Journal of Crystal Growth, 1980, v. 48, p. 125 131

[23] Grootjans, A. P., and Ten Klooster, W. P. *Changes of ground water regime in wet meadows.* Acta botanica neerlandica, 1980, 29(5/6), 541-554.

[24] Gunter, W. D., Perkins, E. H. McCann T. J. *Aquifer disposal of CO2-rich gases: reaction design for added capacity* Energ. Convers. Manage., 1993, 34, 941948.

[25] Hammes, F., and W. Verstraete *Key roles of pH and calcium metabolism in microbial carbonate precipitation* Rev. Environ. Sci. Biotechnol., 2002, 1, 37.

[26] Hilgers, C., and J. L. Urai *Experimental study of syntaxial vein growth during lateral fluid flow in transmitted light: first results* Journal of Structural Geology, 2002, 24(67), 10291043.

[27] Holloway, S. *Underground sequestration of carbon dioxidea viable greenhouse gas mitigation option* Energy, 2005, 30(11), 2318-2333.

[28] Hong, K. S., Lee, H. M., Bae, J. S., Ha, M. G., Jin, J. S., Hong, T. E., ... and Jeong, E. D. *Removal of heavy metal ions by using calcium carbonate extracted from starfish treated by protease and amylase.* J Anal Sci Technol, 2011, 2(2), 75-82.

[29] Hu, Y. F., Carter, J. G., and Blake, R. J. *The Effect of the Grid Aspect Ratio on the Convergence of Parallel CFD Algorithms* Parallel Computational Fluid Dynamics' 95: Implementations and Results Using Parallel Computers, 1996, 289.

[30] Huijgen, W. J. J., Comans, R. N. J. *Carbon dioxide sequestration by mineral carbonation. Literature Review (No. ECN-C–03-016)* Energy research Centre of the Netherlands ECN., 2003.

[31] Jones, T. A., Detwiler R. L. *Effects of mineral heterogeneity on precipitation-induced flow alteration in porous and fractured media* Manuscript submitted for publication.

[32] Kamkha, M.A., Sibiryakov, P.B., and Bizyaev, V.L *Effect of pH on the Kinetics of Mass Crystallization of Calcium Carbonate* Kinetics and Catalysis, 1989, v. 30, n.1, p. 62 67.

[33] Kang, Q., P. C. Lichtner, and D. Zhang. *Lattice Boltzmann pore- scale model for multicomponent reactive transport in porous media* J. Geophys. Res., 2006, 111, B05203, doi:10.1029/2005JB003951.

[34] Kays, W. M. *Convective Heat and Mass Transfer* McGraw-Hill, New York., 1966, 387 pp.,

[35] Kessler, T. J., and Harvey, C. F. *Global flux of carbon dioxide into groundwater* Geophysical research letters, 2001, 28(2), 279-282.

[36] Krevor, S., Blunt, M. J., Benson, S. M., Pentland, C. H., Reynolds, C., Al-Menhali, A., and Niu, B. *Capillary trapping for geologic carbon dioxide storageFrom pore scale*

physics to field scale implications. International Journal of Greenhouse Gas Control, 2015, 40, 221-237.

[37] Lanting, B., and Barfett, J. *Encapsulated calcium carbonate suspensions: a drug delivery vehicle sensitive to ultrasound disruption.* McGill Journal of Medicine, 2006, 9(2), 108.

[38] Lasaga, A.C. *Rate laws in chemical reactions. In: Lasaga, A.C., Kirkpatrick, R.J. (Eds.)* Kinetics of Geochemical Processes: Mineralogical Society of America, 1981, vol. 8, pp. 135169.

[39] Lee, S., Wi, H. S., Jo, W., Cho, Y. C., Lee, H. H., Jeong, S. Y., ... and Lee, G. W. *Multiple pathways of crystal nucleation in an extremely supersaturated aqueous potassium dihydrogen phosphate (KDP) solution droplet.* Proceedings of the National Academy of Sciences, 2016, 113(48), 13618-13623.

[40] Lee, Y.-J., and J. W. Morse *Calcite precipitation in synthetic veins: implications for the time and fluid volume necessary for vein filling* Chemical Geology, 1999, 156(14), 151170.

[41] Lowenstam, H. A. *Factors affecting the aragonite: calcite ratios in carbonate-secreting marine organisms* The Journal of Geology, 1954, 62(3), 284-322.

[42] Maruvada, S., Liu, Y., Soneson, J. E., Herman, B. A., and Harris, G. R. *Comparison between experimental and computational methods for the acoustic and thermal characterization of therapeutic ultrasound fields.* The Journal of the Acoustical Society of America, 2015, 137(4), 1704-1713. Chicago

[43] Meakin, P., and Tartakovsky, A. M. *Modeling and simulation of porescale multiphase fluid flow and reactive transport in fractured and porous media.* Reviews of Geophysics, 2009, 47(3).

[44] Metz, B., Davidson, O., de Coninck, H. C., Loos, M. Meyer, L. A. *Carbon Dioxide Capture and Storage* IPCC Special Report, 2005, 197-265.

[45] Nancollas, G.H. and Reddy, M.M. *The Crystallization of Calcium Carbonate: II. Calcite Growth Mechanism* Journal of Colloid and Interface Science, 1971, v. 37, n. 4, p. 824 830.

[46] NASA *The slow carbon cycle.* Retrieved from https://earthobservatory.nasa.gov/Features/CarbonCycl

[47] Nielsen, A.E. *Electrolyte crystal-growth mechanisms.* Journal of Crystal Growth, 1984, 67 (2), 289310.

[48] OpenCFD Ltd (ESI Group) *About OpenFOAM* 2004, Retrieved from http://www.openfoam.com/

[49] OpenFOAM guide *The SIMPLE algorithm in OpenFOAM.* 2014, Retrieved from https://openfoamwiki.net/index.php/OpenFOAM-guide

[50] Parsiegla, K. I., and Katz, J. L. *Calcite growth inhibition by copper (II): II. Effect of solution composition.* Journal of Crystal Growth, 2000, 213(3), 368-380.

[51] Railsback, L.B. *Some Fundamentals of Mineralogy and Geochemistry.* retrieved from http://www.gly.uga.edu/railsback/FundamentalsIndex.html.

[52] Razowska-Jaworek, L. *Calcium and magnesium in groundwater: occurrence and significance for human health.* CRC Press, 2014.

[53] Rightmire, C. T., and Hanshaw, B. B. *Relationship between the carbon isotope composition of soil CO2 and dissolved carbonate species in groundwater.* Water Resources Research, 1973, 9(4), 958-967.

[54] Somani, R. S., Patel, K. S., Mehta, A. R., and Jasra, R. V. *Examination of the polymorphs and particle size of calcium carbonate precipitated using still effluent (ie, CaCl2+*

NaCl solution) of soda ash manufacturing process. Industrial and engineering chemistry research, 2006, 45(15), 5223-5230.

[55] Smith, Stuart A. et al. *Ground Water Hydrology for Water Well Contractors.* Dublin, OH: National Ground Water Association (NGWA,)., 1980, Chapter 23.

[56] Starchenko, V., Marra, C. J., and Ladd, A. J. *Threedimensional simulations of fracture dissolution* Journal of Geophysical Research: Solid Earth, 2016, 121(9), 6421-6444.

[57] Steefel, C. I., D. J. DePaolo, and P. C. Lichtner. *Reactive transport modeling: An essential tool and a new research approach for the Earth sciences, Earth Planet* Sci. Lett., 2005, 240, 539558.

[58] Teng, H.H., Dove, P.M., and De Yoreo, J.J. *Kinetics of Calcite Growth: Surface Processes and Relationships to Macroscopic Rate Laws* Geochimica et Cosmochimica Acta, 2000, v. 64, p. 2255 2266.

[59] The Carbon Cycle and Earth's Climate *Information sheet for Columbia University Summer Session 2012 Earth and Environmental Sciences Introduction to Earth Sciences I* Retrieved from http://www.columbia.edu/ vjd1/carbon.htm

[60] The OpenFOAM Foundation. *OpenFOAM user guide version 4.0.* Retrieved from http://foam.sourceforge.net/docs/Guides-a4/OpenFOAMUserGuide-A4.pdf

[61] Tartakovsky, A. M., G. Redden, P. C. Lichtner, T. D. Scheibe, and P. Meakin *Mixing-induced precipitation: Experimental study and multiscale numerical analysis* Water Resources Research, 2008, 44(6), n/an/a.

[62] Torrance, K. E. *Comparison of finite-difference computations of natural convection* Journal of research of the National Bureau of Standards, 1968, 72(4), 281-301.

[63] Tracy, S. L., Williams, D. A., and Jennings, H. M. *The growth of calcite spherulites from solution: II. Kinetics of formation.* Journal of Crystal Growth, 1998, 193(3), 382-388.

[64] Versteeg, H. K., and Malalasekera, W. *An introduction to computational fluid dynamics: the finite volume method* Pearson Education, 2007

[65] Washington *Rulemaking: Chapter 173-407 WACCarbon dioxide mitigation program for fossil-fueled thermal electric generating facilities and Chapter 173-218 WACUnderground injection control program.* 2007, Retrieved from http://www.ecy.wa.gov/laws-rules/ activity/wac173407-218.html

[66] Weller, M., Overton, T., Rourke, J., Armstrong, F. *Inorganic chemistry* Oxford University Press, USA., 2014.

[67] Zhang, Y., Dawe, R. *The kinetics of calcite precipitation from a high salinity water* Applied Geochemistry, 1998, 13(2), 177-184.